Available online at www.CivileJournal.org

Civil Engineering Journal

(E-ISSN: 2476-3055; ISSN: 2676-6957)

Vol. 12, No. 06, June, 2026

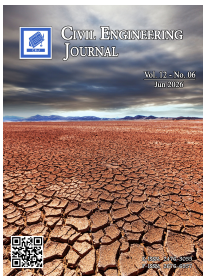

Effect of Regional Topography on Ground Motion Amplification Factors

Qirui Luo [1], Shixing Zhao [1*], Yan Wang [2], Jun Xiong [3], Dandan Wu [4], Min Zhang [5]

[1] *Sichuan Provincial Architectural Design and Research Institute, Chengdu 610041, China.*

[2] *Sichuan Provincial Construction Science and Technology Development and Information Center, Chengdu, 610042, China.*

[3] *Sichuan Xinchuan Engineering Testing Co., Ltd., Chengdu, Sichuan 610095, China.*

[4] *Ganzi Prefecture Construction Engineering Quality and Safety Supervision Station, Kangding 626000, China.*

[5] *School of Civil Engineering and Geomatics, Southwest Petroleum University, Chengdu 610500, China.*

Received 13 March 2026; Revised 16 May 2026; Accepted 18 May 2026; Published 01 June 2026

Abstract

This study systematically investigates how regional topography influences ground motion amplification factors (GMAFs) and clarifies the differences between isolated and complex terrains. Three-dimensional models with viscoelastic artificial boundaries, validated by centrifuge experiments, were used to simulate single-, double-, and regional topographies. The results show significant quantitative differences: for an isolated ridge, the peak acceleration GMAF reaches 3.69 at vertical incidence, while regional topography reduces this by more than 20% owing to ridge interaction effects. Increasing the soil elastic modulus from 150 to 250 MPa resulted in a 204% increase in peak acceleration in the X-direction. Notably, the GMAFs for acceleration, velocity, and displacement exhibited distinct directional variations, with vertical amplification showing the greatest dispersion. The key finding of this study is that the surrounding terrain mitigates the whipping effect of an isolated ridge, and that GMAF assessments must be conducted directionally rather than as a single combined value. These findings underscore the need for separate directional analyses in seismic design codes for mountainous regions.

Keywords: Topographic Effect; Regional Topography; Three-Dimensional Modeling; Viscoelastic Artificial Boundary.

1. Introduction

The ground motion amplification factor (GMAF), which quantifies the modification of peak acceleration, velocity, and displacement during seismic wave propagation, is a fundamental parameter in earthquake engineering and seismic hazard assessment [1-5]. Extensive field observations following major earthquakes have consistently demonstrated that topographic irregularities can significantly alter ground-motion characteristics, with seismic wave energy often concentrated at ridge crests and reflected within narrow canyons [6-8]. Despite the widespread recognition of topographic effects, the quantitative characterization of the GMAF across complex regional-scale terrains remains an unresolved challenge, primarily because of the inherent limitations of simplified analytical models and idealized experimental configurations used in prior investigations.

* Corresponding author: 316458931@qq.com

https://doi.org/10.28991/CEJ-2026-012-06-04

Previous studies on topographic amplification have predominantly focused on isolated or geometrically simplified slope configurations. For instance, Lee et al. [9] conducted geotechnical centrifuge experiments on simplified idealized single-sided slope models and demonstrated that topographic amplification at the crest is strongly frequency dependent, with significant enhancement when topographic and site resonant frequencies converge. This indicates that conventional one-dimensional site response analyses may underestimate seismic demands near slope crests. Li et al. [10] conducted parametric numerical simulations on idealized three-dimensional slope models and found that topographic amplification decreases with increasing soil shear wave velocity, and that vertical amplification can exceed horizontal amplification, suggesting that simplified 2D analyses may underestimate seismic demands in soft soil sites. Tai et al. [11] conducted shaking-table tests on isolated jointed rock slopes and revealed that the dynamic amplification effect was highly dependent on the proximity of the excitation frequency to the natural frequency of the slope. When the two frequencies were close, the amplification was most pronounced. Wang et al. [12] performed numerical stress-deformation analyses on idealized multilayer earth slopes and demonstrated that longer-duration ground motions significantly increase permanent slope displacements, with the probability of moderate damage reaching 20%.

Although these studies have substantially advanced our understanding of topographic amplification, a critical examination reveals several persistent limitations. First, most investigations have been constrained to two-dimensional profiles or isolated three-dimensional features, thereby precluding the analysis of wave field interactions among adjacent ridges that characterize genuine mountainous terrains. Second, the potential mutual influence of neighboring topographic features on the GMAF remains poorly quantified; specifically, it is unclear whether the presence of surrounding ridges mitigates or exacerbates the amplification experienced at a given location. Third, existing parametric analyses have primarily focused on individual topographic attributes, such as slope angle, height, or material properties, without systematically addressing the compounded effects inherent to regional topography comprising multiple ridges of varying elevations and spatial distributions [13-15]. Consequently, the extrapolation of findings derived from idealized single-ridge models to complex regional settings introduces considerable uncertainty into seismic design provisions and site selection practices.

To address these research gaps, this study presents a systematic numerical investigation of the influence of regional topography on the GMAF. The specific objectives of this study are threefold: (1) to quantify the sensitivity of the GMAF to the elastic modulus, topographic height, and slope angle for single-ridged topography using a validated three-dimensional finite element modeling framework; (2) to elucidate the interaction mechanisms between adjacent ridges by analyzing double-ridged configurations with varying spacing and relative heights; and (3) to evaluate the compounded topographic effects within realistic regional settings characterized by randomly distributed ridge heights. The modeling approach incorporated image recognition techniques for topographic surface generation and viscoelastic artificial boundaries for wave propagation. Its validity was confirmed through a comparison with published centrifuge experimental data. The findings derived from this investigation are intended to provide a refined quantitative basis for seismic site characterization and structural design in mountainous regions, while simultaneously highlighting the necessity of directional and region-specific amplification assessments.

2. Finite Element Model and Verification

2.1. Workflow of the Numerical Methodology

To provide a clear overview of the research procedure, a flowchart summarizing the key steps of the numerical methodology is presented in Figure 1. The workflow consists of four principal stages: (1) three-dimensional topography modeling using image recognition techniques and Python-based coordinate transformation; (2) implementation of viscoelastic artificial boundaries and equivalent nodal force input to simulate semi-infinite domain conditions; (3) validation of the finite element model against published centrifuge experimental data; and (4) analyses of the parametric GMAF for single-ridged, double-ridged, and regional topographies. A detailed description of each component is provided in subsequent subsections.

2.2. Numerical Model Setup

All finite element simulations were performed using ABAQUS. Three-dimensional topography models were constructed using an image-recognition-based approach, with viscoelastic artificial boundaries applied to all lateral and bottom faces of the computational domain to simulate the radiation damping of the semi-infinite foundation. Seismic excitation was introduced as an equivalent nodal force on the boundary nodes. The computational domain was extended laterally and vertically at least 2.5 times the maximum ridge height from the crest to minimize boundary disturbances. Eight-node elements (C3D8R) were used for spatial discretization, with the mesh refined sufficiently near the ridge crest, within the limits of the available computational capacity, to adequately resolve wave propagation. The total number of elements varied with the topographic complexity.

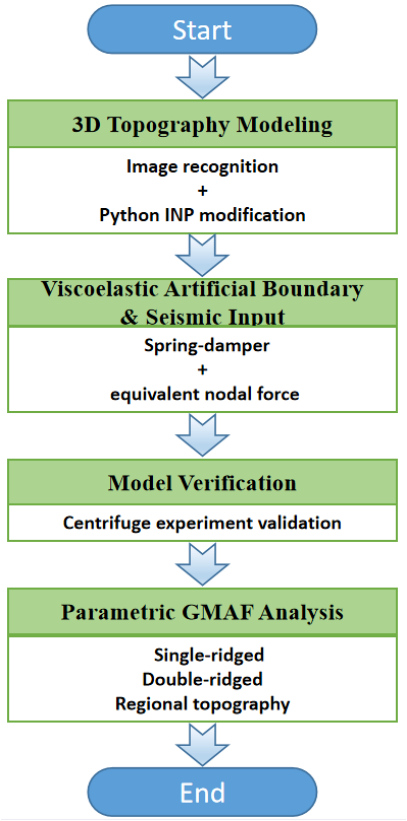

Figure 1. Flowchart of the numerical methodology for topographic effect analysis

2.3. Three-Dimensional Modeling Method

Modeling ridged topography serves as a crucial foundation for three-dimensional finite element analysis. However, Abaqus's in-built tools have been shown to be inadequate for constructing such complex models. This study proposes an image recognition technology for three-dimensional ridged topography modeling. The overall process is shown in Figure 2, and the main steps are as follows:

- Based on the size of the analyzed area, a cuboid model was established as the foundation and output in INP file format, as shown in Figure 2-b. This file contains nodes, elements, and set information.
- According to the coordinates of the topographic feature points, MATLAB was used to interpolate and fit to produce a black-and-white false elevation map. These maps are shown in Figure 2-c.
- The model information in the INP file was parsed using Python. The entire black-and-white elevation map was scanned to obtain the range of pixel point R in the image. Following normalization, the value was stored in a temporary list with data format (x, y, α);
- The Z-axis coordinates of all nodes in the model were adjusted based on the maximum elevation difference of the actual topography. A new INP file with the updated node coordinates and other content was generated. The final model is shown in Figure 2-d.

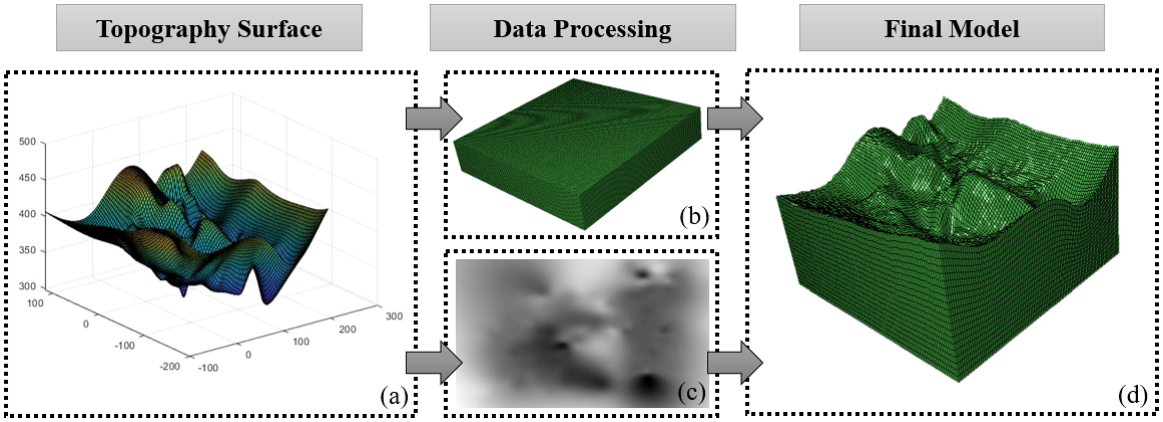

Figure 2. The modeling process of three-dimensional topography

The accuracy of the image recognition modeling is primarily controlled by two factors: the pixel resolution of the false elevation map, and the interpolation method. In this study, a map resolution of 1024 × 1024 pixels was used to ensure that the spatial discretization of the topographic surface was finer than 1.0 m in the horizontal direction. Grayscale-to-elevation conversion was performed using linear interpolation between the pixel nodes. Potential sources of modeling errors include (1) minor geometric smoothing introduced during pixel-node coordinate mapping, particularly in regions with extremely steep local discontinuities, and (2) truncation of small-scale surface roughness owing to finite pixel resolution.

2.4. Viscoelastic Artificial Boundary and Equivalent Node Force

Viscoelastic artificial boundaries have been widely employed in numerical simulations of seismic responses at sites owing to their inherent advantages, making them an important method for converting infinite foundations into finite foundations [16-18]. The modeling method aims to simulate the interaction between a finite and an infinite foundation by setting spring elements. The calculated stiffness and damping coefficients of the spring are listed in Table 1.

Table 1. Spring coefficient

Spring	Tangential boundary	Normal boundary
Stiffness coefficient	$\alpha_T \frac{G}{R}$	$\alpha_N \frac{G}{R}$
Damping coefficient	ρC_s	ρC_p

where, α_T and α_N are tangential and normal viscoelastic artificial boundary parameters, respectively. C_s and C_p are S-wave and P-wave velocities, respectively. G and $\rho$are the shear modulus and density of foundation media, R is the distance from the wave source to the artificial boundary. Additionally, a reasonable seismic wave inputting mode was essential to ensure accurate site seismic simulation analysis. The equivalent node force calculation method is given in Huang et al. [19], and the SH-wave calculation formula is shown in Equation 1.

$$F = A_l(K_{li}u_{li}^f + C_{li}\dot{u}_{li}^f + \sigma_{li}^f) \tag{1}$$

where, u_{li}^f, $\dot{u}_{li}^f$, and σ_{li}^f are the displacement, velocity, and stress of the corresponding nodes, respectively. They require conversion from the local coordinate system. The related calculation formulas are given in Equations 2 to 4. $[\sigma_{ij}^l]$ was calculated by Equation 5, and $\tau_{\mathrm{yz}}^l = \tau_{\mathrm{zy}}^l = -\frac{G}{c_s}\dot{u}(t-\Delta t)$. T_1 and T_2 are transformation matrices between the local and global coordinates of the incident and reflected waves.

$$[U] = \sum_{i=1}^{2} T_i [U_i] \tag{2}$$

$$[\dot{U}] = \sum_{i=1}^{2} T_i [\dot{U}_i] \tag{3}$$

$$[\sigma_{ij}] = \sum_{i=1}^{2} [T_l]^T [\sigma_{ij}^l] [T_l] \tag{4}$$

$$[\sigma_{ij}^l] = \begin{bmatrix} 0 & 0 & 0 \\ 0 & 0 & \tau_{\mathrm{yz}}^l \\ 0 & \tau_{\mathrm{zy}}^l & 0 \end{bmatrix} \tag{5}$$

$$T_1 = \begin{bmatrix} \frac{\cos\alpha\cos\beta}{\sqrt{\cos^2\alpha+\cos^2\gamma}} & -\sqrt{\cos^2\alpha+\cos^2\gamma} & \frac{\cos\gamma\cos\beta}{\sqrt{\cos^2\alpha+\cos^2\gamma}} \\ \cos\alpha & \cos\beta & \cos\gamma \\ -\frac{\cos\gamma}{\sqrt{\cos^2\alpha+\cos^2\gamma}} & 0 & \frac{\cos\alpha}{\sqrt{\cos^2\alpha+\cos^2\gamma}} \end{bmatrix} \tag{6}$$

$$T_2 = \begin{bmatrix} -\frac{\cos\alpha\cos\beta}{\sqrt{\cos^2\alpha+\cos^2\gamma}} & -\sqrt{\cos^2\alpha+\cos^2\gamma} & -\frac{\cos\gamma\cos\beta}{\sqrt{\cos^2\alpha+\cos^2\gamma}} \\ \cos\alpha & -\cos\beta & \cos\gamma \\ -\frac{\cos\gamma}{\sqrt{\cos^2\alpha+\cos^2\gamma}} & 0 & \frac{\cos\alpha}{\sqrt{\cos^2\alpha+\cos^2\gamma}} \end{bmatrix} \tag{7}$$

2.5. Model Verification

To validate the modeling method, an experiment from Sun et al. [20] was selected and compared with a simulation. The specimen was a slope model with height 14.5 m. Earthquake wave was incident vertically from the bottom. Figure 3 shows the acceleration time-history curve of El-centro wave. Table 2 lists the material parameters of the simulation, which are based on the material properties of the experimental specimen.

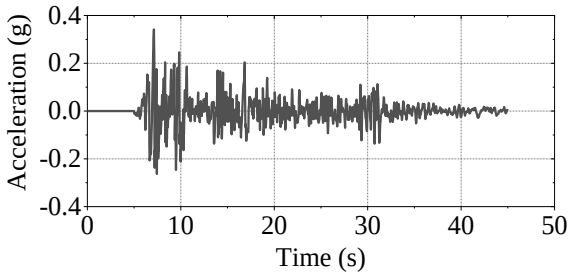

Figure 3. Acceleration time-history curve of El-centro wave

Table 2. Modeling parameter [20]

Material parameter	Value
Density (kg/m^3)	1.83
Damping (%)	0.2
Friction angle (°)	41
Dilation angle (°)	4
Bulk modulus (kPa)	2.391e5
Poisson's ratio	0.25

Through a time-history analysis, the acceleration curves of the nodes with H = 0 m and H = 13 m were obtained, and a comparison between the experimental data and simulation results is presented in Figure 4. In the simulation, the peak accelerations of nodes at H = 0 m and H = 13 m were -1.05 m/s^2 and -2.01 m/s^2, respectively. Meanwhile, in the experiment, the peak accelerations of nodes at H = 0 m and H = 13 m were -1.05 m/s^2 and -2.06 m/s^2, respectively. The errors were only 0.34% and 2.48%, respectively, indicating that the simulation method was valid, and that the seismic response process of the experimental specimen could be restored.

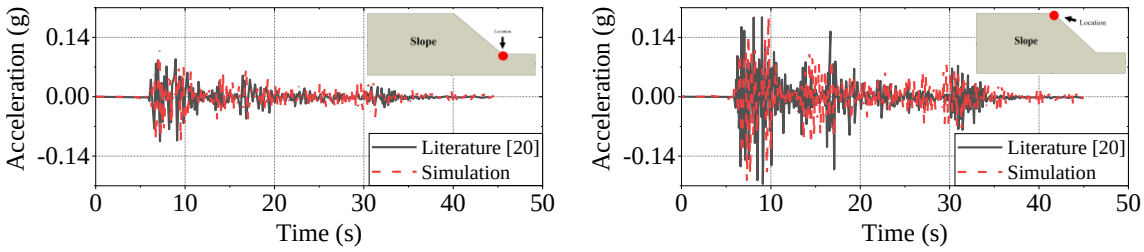

(a) H = 0 m **(b) H = 13 m**

Figure 4. Result comparison

While the validation relies on a single experimental case, this scenario adequately captures the fundamental wave propagation behavior toward a slope crest, which is the primary physical process governing topographic amplification in this study. The close agreement thus obtained confirms that the modeling approach is suitable for the parametric analyses undertaken herein. Further validation against a broader set of experiments may be pursued in future studies to enhance the generality.

3. GMAF Analysis of Single-Ridged Topography

Prior to the parametric analyses, the selected ranges of the variables – elastic modulus from 150 MPa to 350 MPa, ridge height from 50 m to 150 m, and slope angle from 15 to 75 – were chosen to broadly span the conditions encountered in medium-relief mountainous terrains. These values are not intended to correspond to specific lithologies but rather to facilitate a systematic exploration of topographic amplification trends across a realistic parameter space.

3.1. Elastic Modulus

The elastic modulus is a key factor influencing the propagation velocity of seismic waves on ground motion. A time-history analysis was performed on specimens with different elastic moduli. The analysis results and model diagrams are presented in Table 3 and Figure 5, respectively.

Table 3. Ground motion data of the specimens with different elastic modulus

	Elastic modulus (MPa)	Acceleration (m/s^2)				Velocity (m/s)				Displacement (m)			
		M	X	Y	Z	M	X	Y	Z	M	X	Y	Z
E150-max	150	1.79	0.79	0.40	0.23	0.44	0.34	0.05	0.10	0.52	0.04	0.02	0.52
E200-max	200	1.66	1.32	0.38	0.27	0.34	0.36	0.07	0.10	0.54	0.04	0.02	0.54
E250-max	250	3.27	2.40	0.94	0.67	0.43	0.37	0.13	0.13	0.95	0.04	0.02	0.95
E300-max	300	2.56	2.14	0.72	0.27	0.35	0.22	0.03	0.10	0.56	0.04	0.02	0.56
E350-max	350	1.52	0.94	0.66	0.93	0.48	0.36	0.15	0.26	1.11	0.05	0.03	1.11

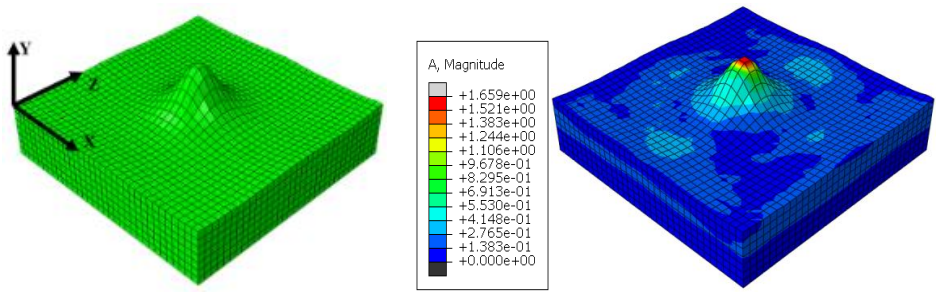

(a) coordinate axis **(b) ground motion in the magnitude direction**

Figure 5. Model diagram

It should be noted that the topographic heights of all specimens were set at 100 m, and the data included results in four directions (Magnitude, X-axis, Y-axis, and Z-axis). Based on the analysis results, the X axis exhibited the most intense ground motion among the three principal axes. The elastic modulus of the foundation influenced the ground motion state. When the elastic modulus of the foundation increased from 150 MPa to 250 MPa, the peak acceleration in X-direction increased from 0.79 m /s^2 to 2.40 m /s^2. When the elastic modulus of the foundation increased from 250 MPa to 350 MPa, the peak acceleration in X-direction decreased from 2.40 m /s^2 to 1.52 m /s^2. The nonmonotonic variation in acceleration was due to the shift in the resonance frequencies of the ridge relative to the dominant frequency of the input motion as the stiffness changed.

For a more comprehensive analysis, Figure 6 shows the GMAF histogram. The effect of different elastic moduli on the GMAF essentially reflects the variation law of ground motion under different geological conditions. The GMAF for acceleration was found to be higher than those for velocity and displacement. According to the seismic code [21], acceleration is the primary parameter for seismic response evaluation. The GMAF of the acceleration in the y-axis (vertical) direction exhibited a significantly greater magnitude than that observed in the other directions, which is an evident phenomenon. However, the previous analysis indicated that the X axis experienced the most intense acceleration, in contrast to the GMAF. It could be illustrated that the focus of GFAM in the vertical direction should be emphasized. In addition, the topographic effect was alleviated in topographies with harder soils. For instance, the GMAF values of specimens oriented along the X-axis with elastic moduli of 200 MPa and 350 MPa were determined to be 1.38 and 1.28, respectively. Therefore, for hard ground, the amplification factor can be appropriately decreased in the structural design.

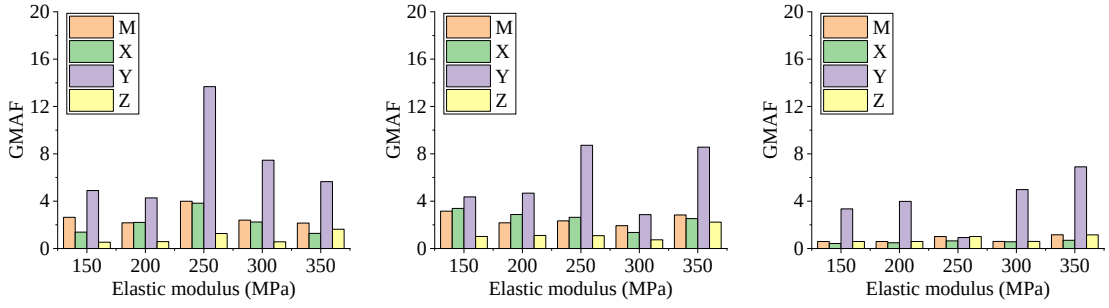

(a) Acceleration **(b) Velocity** **(c) Displacement**

Figure 6. GMAF histogram

The observed differences among the acceleration, velocity, and displacement GMAFs were noted; however, the underlying physical mechanisms, such as frequency-dependent wave scattering and energy dissipation, require further investigation. The present analysis was primarily observational, and a deeper exploration of these mechanisms is warranted for future work.

3.2. Topographic Height

The ridge height served as the fundamental parameter in investigating topographic effects, and Table 4 presents the analysis results for specimens with varying ridge heights. The ground motion became more intense as the height of the ridges increased; this phenomenon reflected a whipping effect. For instance, the H050 and H150 experienced accelerations of 1.34 m/s^2 and 3.38 m/s^2 in the magnitude direction, respectively, resulting in a significant increase of 252.2%. In addition, it was also found that the acceleration increased almost linearly with an increase in ridge height, and more models should be developed to examine this hypothesis.

Table 4. Ground motion data of the specimens with different ridged height

	Ridged height (m)	Acceleration (m/s^2)				Velocity (m/s)				Displacement (m)			
		M	X	Y	Z	M	X	Y	Z	M	X	Y	Z
H050-max	50	1.34	0.75	0.43	0.30	0.14	0.20	0.06	0.14	0.94	0.04	0.02	0.94
H075-max	75	2.55	1.92	0.75	0.33	0.27	0.30	0.07	0.12	0.94	0.04	0.02	0.94
H100-max	100	3.22	2.43	0.87	0.50	0.42	0.40	0.11	0.13	0.94	0.04	0.02	0.94
H125-max	125	2.99	1.96	0.94	0.49	0.61	0.56	0.06	0.27	0.95	0.04	0.02	0.95
H150-max	150	3.38	1.98	0.95	0.31	0.93	0.76	0.06	0.16	0.95	0.04	0.02	0.95

Figure 7 illustrates the GMAF histograms for the acceleration, velocity, and displacement. Compared with acceleration, the GMAF values of velocity and displacement were lower. The primary reason was that the GMAF was defined as the ratio of the maximum and original values of the corresponding indicator while exhibiting minimal changes in velocity and displacement. As shown in Figure 7-a, the GMAF of the acceleration was significantly higher than that stipulated by the seismic code (1.6). The application of related coefficients in the code for structural design was found to potentially compromise safety. However, when the height of the ridge increased from 125 to 150 m, there was a decrease in the GMAF of vertical acceleration owing to a shift in the location with the most intense vertical motion.

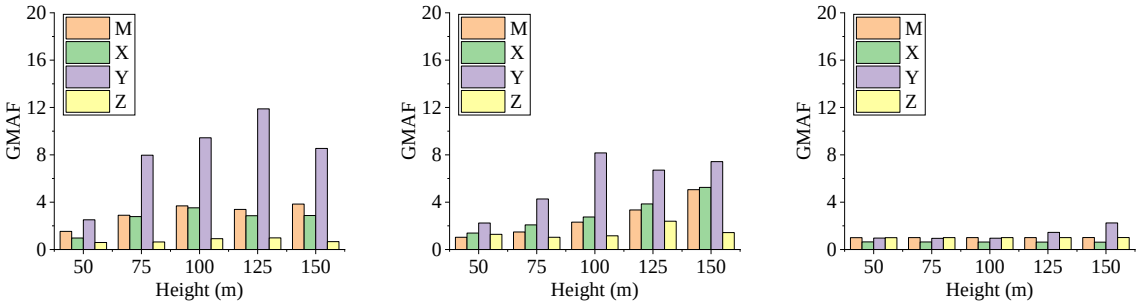

(a) Acceleration **(b) Velocity** **(c) Displacement**

Figure 7. GMAF histogram

3.3. Topographic Slope

The ridged slope is another important research parameter for topographic effects. Table 5 shows the results from our related analysis. All the specimens had a height of 100 m, and the seismic wave was vertically input from the bottom. When the slope did not exceed 30 °, there was minimal variation in the acceleration, velocity, and displacement. The differences in acceleration, velocity, and displacement were 0.27 m/s^2, 0.04 m/s, and 0 m, respectively. When the slope increased from 30 °to 75 °, the differences in the acceleration, velocity, and displacement were 0.61 m/s^2, 0.34 m/s, and 0.01 m. This indicates that the ridged slope had a certain degree of influence on the ground motion.

Table 5. Ground motion data of the specimens with different ridged slope

	Ridged slope (°)	Acceleration (m/s^2)				Velocity (m/s)				Displacement (m)			
		M	X	Y	Z	M	X	Y	Z	M	X	Y	Z
S-15-max	15	2.52	1.98	0.74	0.40	0.30	0.27	0.07	0.14	0.94	0.04	0.02	0.94
S-30-max	30	2.79	2.19	1.01	0.42	0.34	0.31	0.09	0.12	0.94	0.04	0.02	0.94
S-45-max	45	3.22	2.43	0.87	0.50	0.42	0.40	0.11	0.13	0.94	0.04	0.02	0.94
S-60-max	60	3.39	2.61	0.96	0.39	0.71	0.34	0.12	0.14	0.95	0.04	0.02	0.95
S-75-max	75	3.40	2.49	0.88	0.36	0.68	0.39	0.06	0.16	0.95	0.04	0.03	0.95

Figure 8 shows the GMAF histograms of the specimens with different ridged slopes. The GMAFs of the acceleration in the X and magnitude directions exhibited smaller disparities, both of which increased with an increase in the ridged slope. The GMAFs of the Y-direction- and Z-direction accelerations are less correlated with each other. Although the peak accelerations of the specimens with slopes of less than 45 °exhibited slight changes, the GMAF of the acceleration continuously improved as the topographic slope increased. For instance, in the magnitude direction, E150 showed an improvement to 2.86, while E200 and E250 demonstrated even greater improvements at 3.17 and 3.69 respectively. The GMAF value of the acceleration in the vertical direction was also far greater than that in the other directions. Meanwhile, the GMAF value of the vertical acceleration exceeded that of the acceleration in the other directions. Investigation of topographic effects necessitates a distinct examination of the vertical amplification effect. Overall, steeper slopes intensify the wave trapping and constructive interference at the crest. Vertical amplification is influenced more by local curvature than by global slope angle alone.

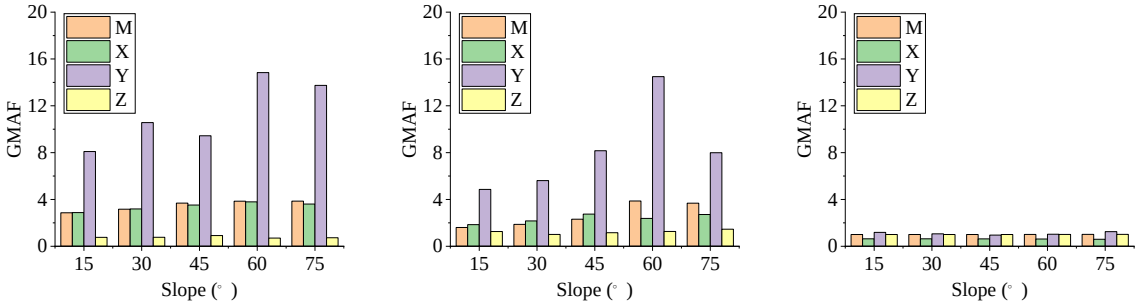

(a) Acceleration **(b) Velocity** **(c) Displacement**

Figure 8. GMAF histogram

4. GMAF Analysis of Double-Ridged Topography

4.1. Equal-Height Ridges

Ridges do not exist in isolation in the actual topography, and their mutual influence requires further investigation. Ridge spacing is a fundamental parameter for distinguishing various topographies. Figure 9 presents the magnitude acceleration cloud images of the specimens at different distances, captured at 10.96 s, with a ridged height of 100 m. The obvious phenomenon was observed that the vibration of ridge top was more intense when the topography owned smaller spacing. For instance, the maximum acceleration observed in the specimens with a spacing of 50 m was 1.22 m/s^2, whereas that in the specimens with a spacing of 150 m was 0.83 m/s^2. This indicates that the interaction between ridges influences the ground motion.

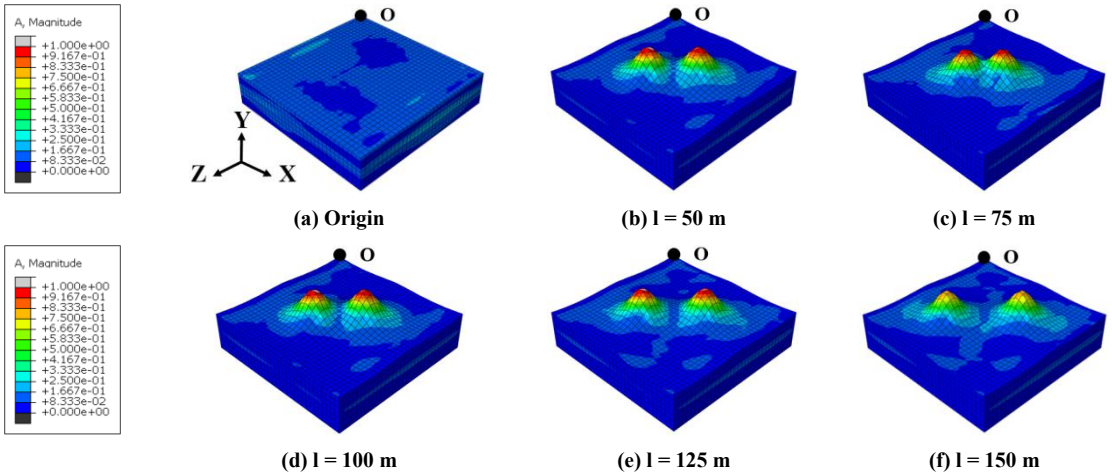

(a) Origin **(b) l = 50 m** **(c) l = 75 m**

(d) l = 100 m **(e) l = 125 m** **(f) l = 150 m**

Figure 9. Acceleration cloud image at 10.96 s

The GMAF value was derived through a conversion based on the acceleration ratio, and the results are illustrated in Figure 10. The point "O" was the origin of coordinates. In the X-direction, the maximum value of GMAF was observed at the top of the ridged topography and increased with increasing ridge spacing. Regarding the vertical seismic action (Y-direction), the maximum value of the GMAF was observed on both sides of the ridged topography. This observation suggests that the areas with the most severe damage may not necessarily be located at the highest points of the ridged topography; this phenomenon warrants further investigation. The EFAM analysis in the Z-direction revealed the absence of highlighted areas, indicating that topographic effects did not occur. For the direction of the magnitude, highlighted areas appeared on the ridge tops, and the maximum was 1.75. This differed from the vertical law (the maximum was

5.14°, and the highlighted areas were not concentrated at the top of the ridge). Thus, to ensure structural safety, the EFAM should consider not only the combined effect of acceleration in the three directions, but also each direction separately.

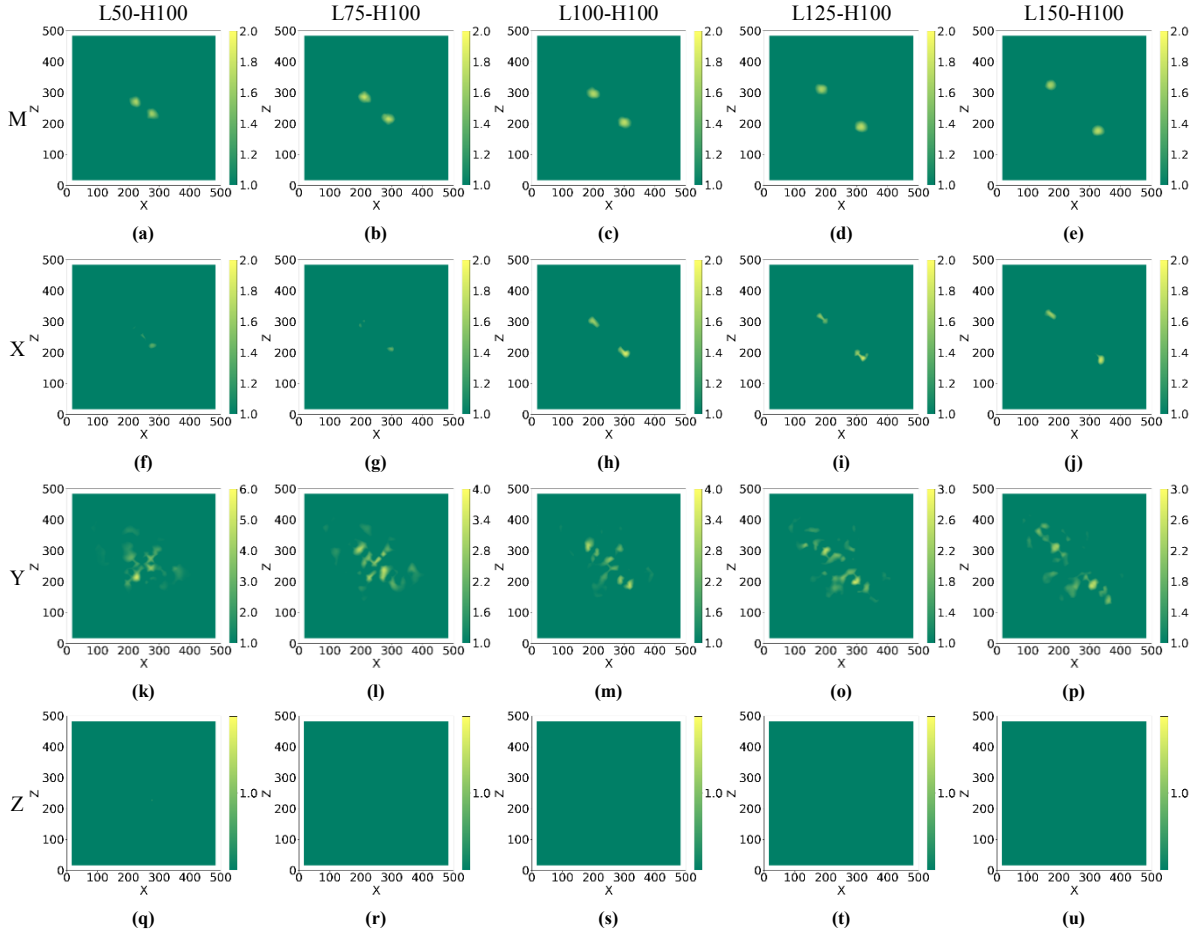

Figure 10. GMAF distribution map of specimens with different ridged spacing

4.2. Original and Lower Ridges

The previous section investigated the topographic effects of ridges with identical heights but varying spacing. In reality, attaining equivalent elevations in mountainous terrains presents a formidable challenge. Hence, the interactions between the ridges of different heights should be investigated. The acceleration cloud images of the specimens with the original and lower ridges at 10.96 s are depicted in Figure 11. The right topography consisted of an original ridge with a height of 100 m, whereas the left topography was characterized by a lower ridge with varying heights ranging from 60 to 100 m. The ridged spacing was 100 m. From the acceleration cloud image, it could be observed that the acceleration of the original ridge top decreased as variable ridged height increased (from 2.82 m/s^2 to 1.75 m/s^2). The analysis in Section 3.2 revealed a noteworthy phenomenon: the peak acceleration of the isolated original ridge reached 3.22 m/s^2. The coexistence of adjacent lower ridges attenuated the vibrational intensity of the original ridge.

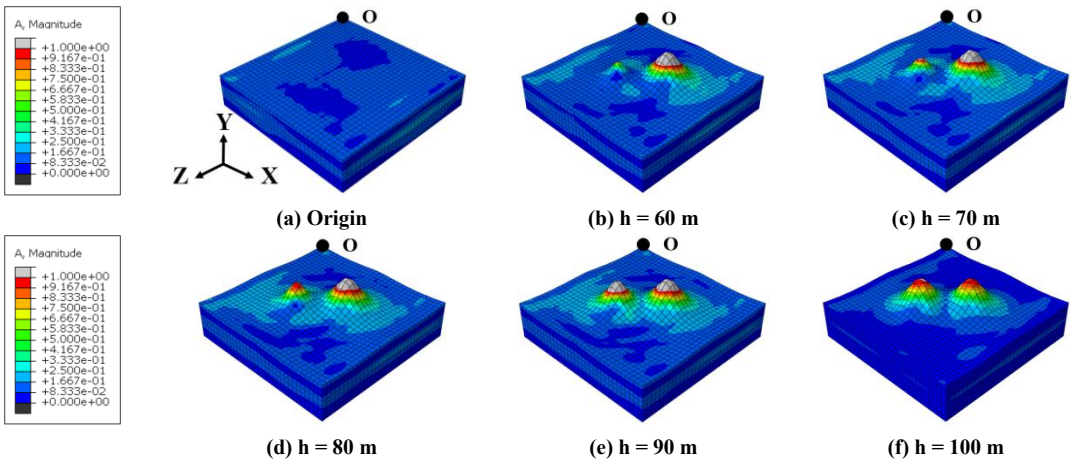

Figure 11. Acceleration cloud image at 10.96 s

Furthermore, Figure 12 shows the GMAF distribution map of the specimens with the original and lower ridges. Compared to specimen H100 in Section 3.2, the GMAF values of the original ridge decreased. The highlight area of GMAF distribution in the vertical direction still exhibited discreteness and unconsecrated phenomenon. Moreover, the GMAF values were significantly higher than those in the other areas. This suggests that separate research in different directions is necessary to investigate the topographic effects. However, the height of the variable ridge in proximity to the original ridge influenced the GMAF of the latter in the direction (from 2.65 1.64). In conclusion, a reduction in the GMAF for structural seismic design can be achieved when the lower ridge is in close proximity to the investigated ridge. The adjacent lower ridge diverts a portion of the incident wave energy, which reduces the energy arriving at the original ridge, thereby mitigating its amplification.

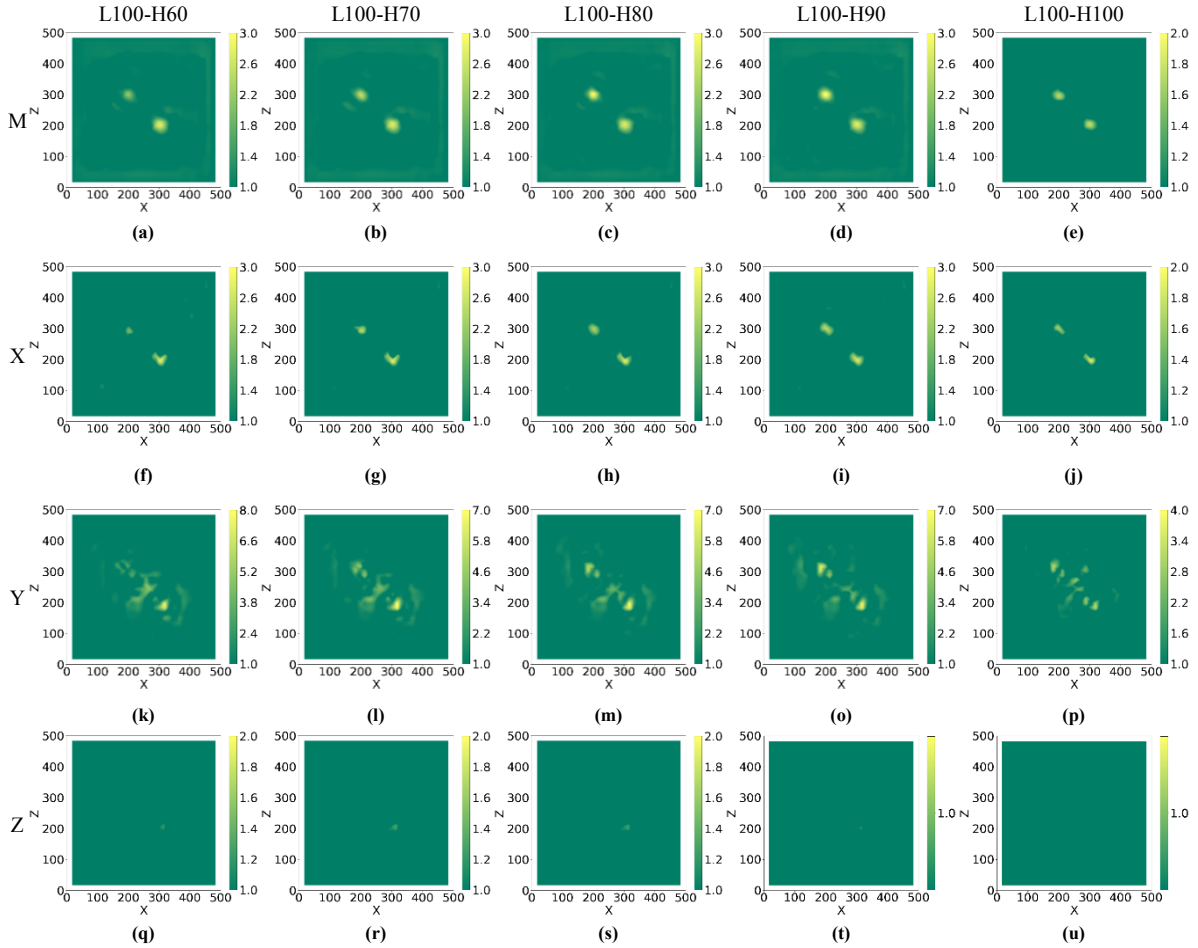

Figure 12. GMAF distribution map of specimens with original and lower ridges

4.3. Original and Higher Ridges

In addition to smaller ridges, there may be more ridges in the actual topography. Figure 13 shows the analysis results for the specimens with the original and higher ridges. The right topography consisted of an original ridge with a height of 100 m, whereas the left topography was characterized by a higher ridge with varying heights ranging from 100 to 140 m. The ridge spacing was set at 100 m. In contrast to the lower ridge law, the model exhibited peak acceleration on the original ridge rather than on a higher ridge. As the number of adjacent ridges increased, the vibration of the original ridge intensified (from 1.75 m/s^2 2.97 m/s^2). Although these accelerations were all below the peak acceleration of the isolated ridge, adhering to a higher ridge reduced the effects of the mountain interactions.

Figure 14 shows the GMAF distribution map of the specimens with the original and higher ridges. The GMAF value reflects the strength of topographic effects. The highlighted area of the GMAF distribution map is concentrated in the region of the ridged top, with the exception of the vertical direction. The GMAF value of the original ridge exhibited a positive correlation with an increase in the adjacent ridge height. For example, when the height of the adjacent ridge is 100 m, the GMAF of the original ridge in the direction of the magnitude is 1.64. When the height of the adjacent ridge was 140 m, the GMAF of the original ridge in the direction was 2.79. It should be explained that the increase in height of the adjacent ridge only mitigated the influence of ridge interaction, but the phenomenon of ridge interaction impeding the topographic effect still persisted (the GMAF of the isolated ridge was 3.69). The presence of a neighboring ridge disrupts the coherent wave field required for strong whipping. As the adjacent ridge increases, the destructive interference is partially diminished, and the response of the original ridge is slightly recovered.

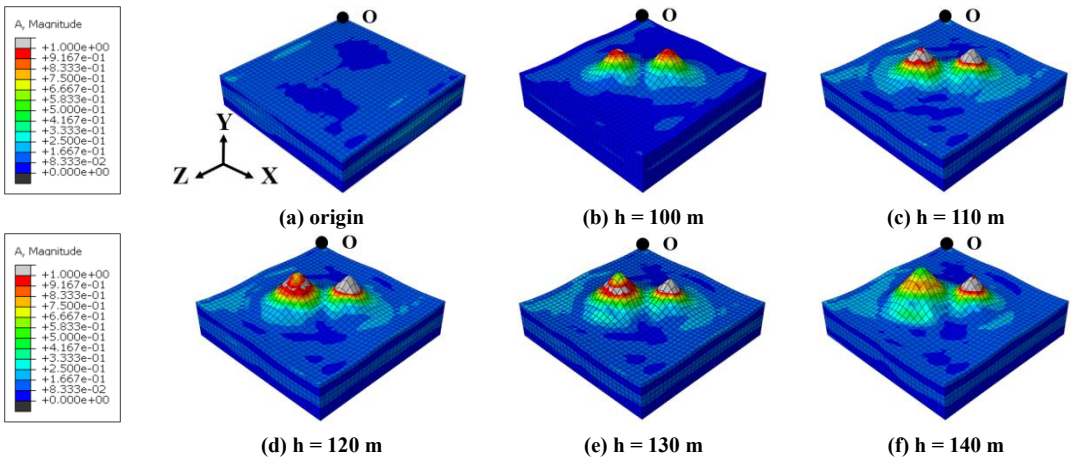

Figure 13. Acceleration cloud image at 10.96 s

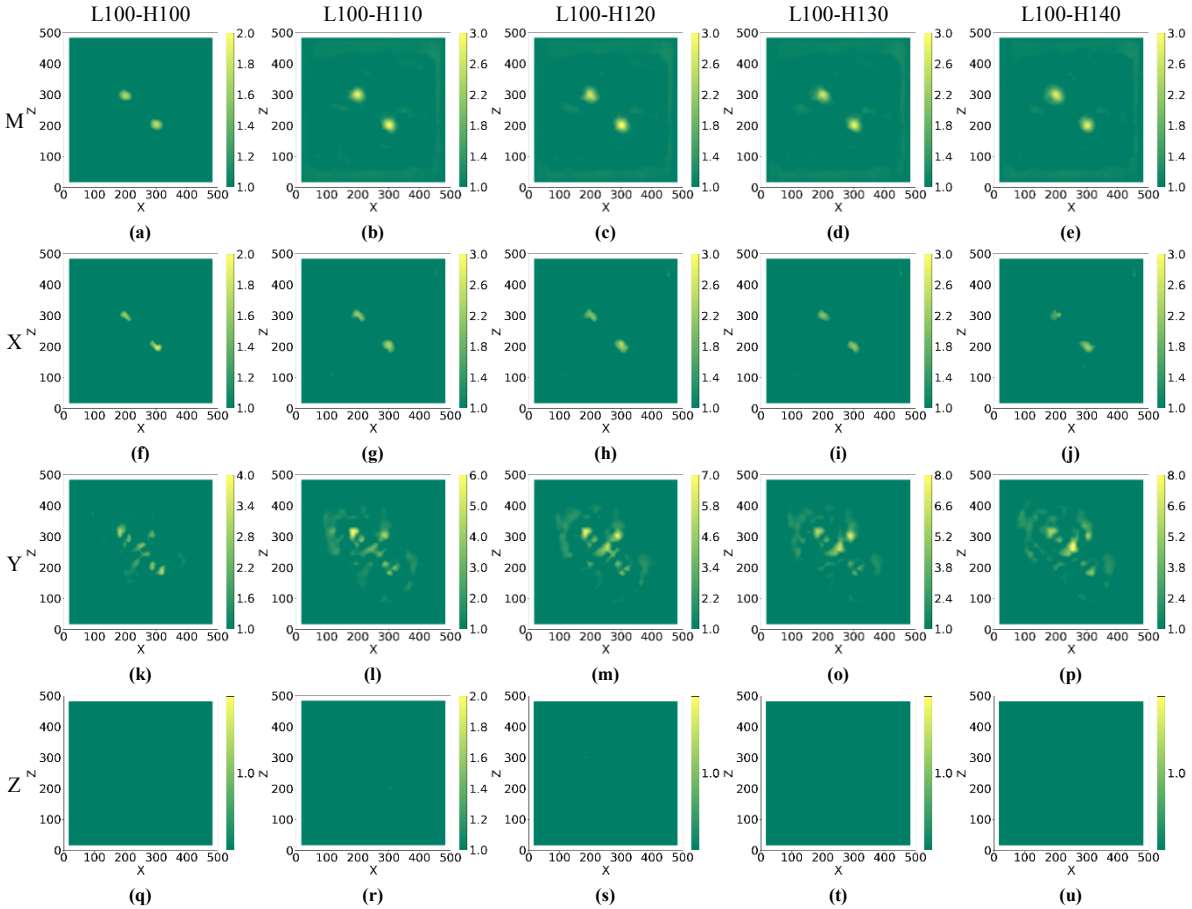

Figure 14. GMAF distribution map of specimens with original and higher ridges

5. GMAF Analysis of Regional Topography

5.1. Equal-Height Ridges

According to the preceding analysis, the interaction between ridges influences the ground motion. In reality, regional topography often encompasses multiple ridges, thus necessitating an exploration of its impact on GMAF. The central ridge of the model had an elevation of 100 m, whereas the regional ridges exhibited a height range within the same interval. Five specimens of the regional topography were established by applying the random function, Figure 15 gave the analysis results of the flat and regional ridge topography. Figure 15-b represents a typical regional ridge, whereas Figure 15-d displays the acceleration time-history curves of the ridged top for the five specimens in the X-direction. It could be observed that the peak acceleration of the central flat topography was 0.73 m/s^2, whereas the range of the peak acceleration of the top ridged topography varied from 1.61 m/s^2 to 2.44 m/s^2. Evidently, the ground motion of a ridged top is influenced by the regional topography with equal elevation, and targeted research should be conducted on different topographic features.

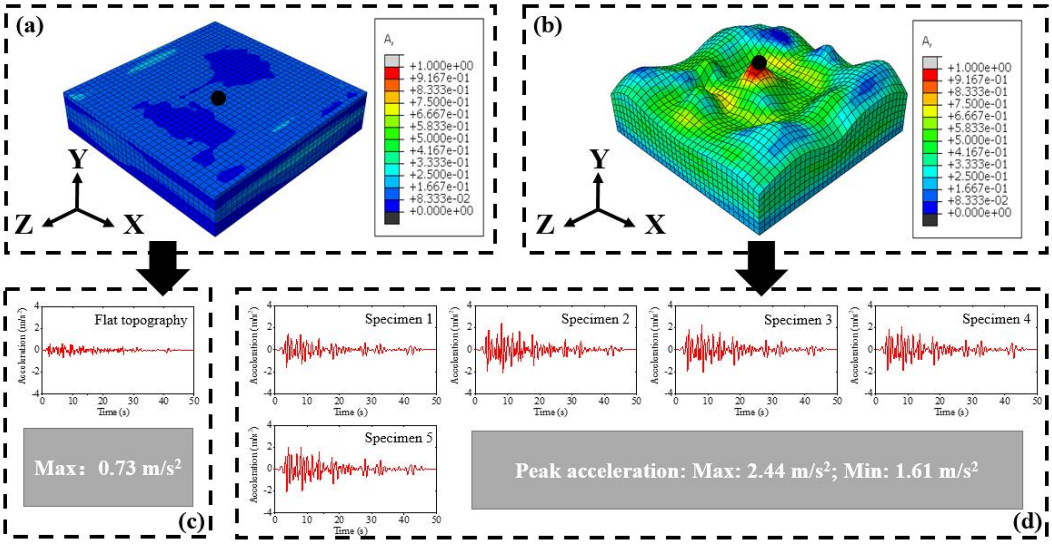

Figure 15. Acceleration time-history curve comparison of 5 specimens with equal-height

Figure 16 illustrates the topographic effects of regional ridge of a typical regional ridge. It is evident that the trend of the height surface diagram differs from that of the acceleration surface diagram. Although there was a ridge of comparable height in the surrounding area, peak acceleration in the X-direction still occurred at the center. Conversely, despite having a height similar to that of the center, the ridges surrounding the model exhibited lower peak accelerations and GMAF values. The rest of the area was found to be relatively unaffected by topographic effects, with the exception of the center. The maximum GMAF value of the central ridge was 2.75 and lower than that of the isolated ridge (3.52). It was illustrated that the interaction between equal-height ridges could mitigate topographic effects.

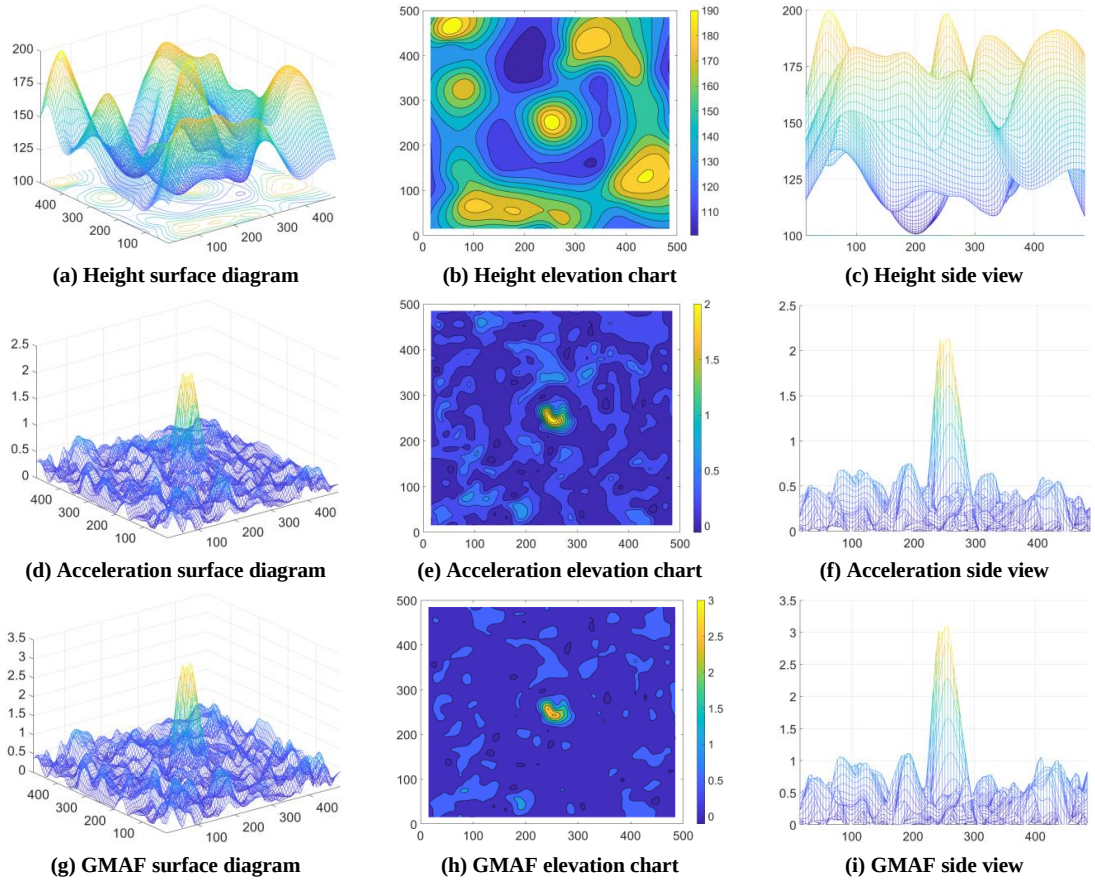

(a) Height surface diagram (b) Height elevation chart (c) Height side view

(d) Acceleration surface diagram (e) Acceleration elevation chart (f) Acceleration side view

(g) GMAF surface diagram (h) GMAF elevation chart (i) GMAF side view

Figure 16. Regional topographic effect of a typical regional ridge (units: m for height; m/s² for acceleration)

5.2. Original and Lower Ridges

Figure 17 shows the analysis results of another situation in which the original ridge was surrounded by lower ridges, and the height of the adjacent ridge was randomly generated from 50 m to 100 m. Based on the analysis results, the peak

accelerations of the five specimens occurred at the top of the central ridge and ranged from 1.90 m/s^2 2.41 m/s^2. Compared to the peak acceleration of the isolated ridge (2.43 m/s^2), the whipping effect of the ridged top surrounded by the lower ridges was mitigated. However, owing to variations in regional topography, the impact on the whipping effect differed accordingly. Additionally, although the range of variation in the peak acceleration for ridges surrounded by lower ridges was lower than that for ridges surrounded by equally high ridges, further specimens are required to elucidate the interaction between the original and lower ridges.

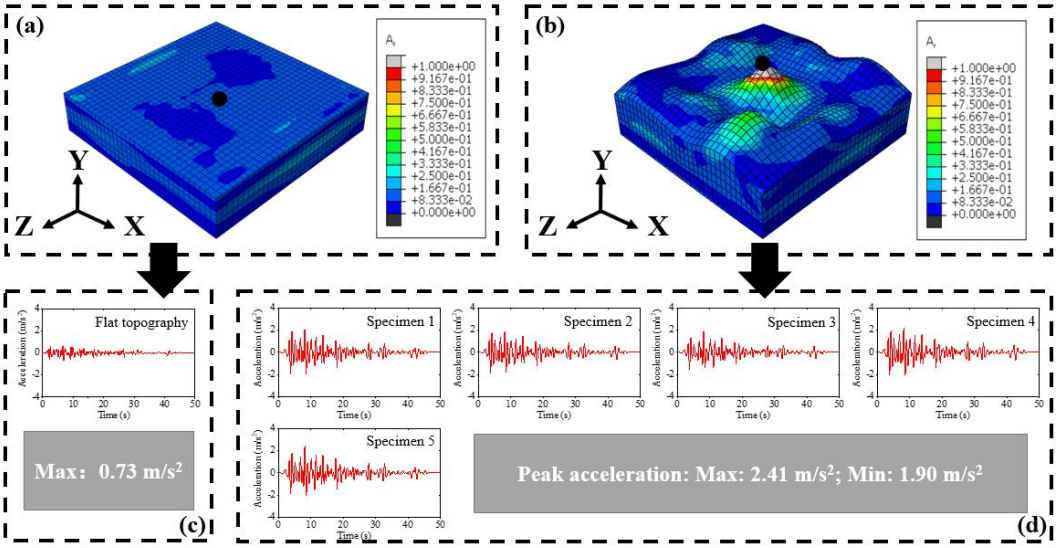

Figure 17. Acceleration time-history curve comparison of 5 specimens

Figure 18 shows the regional topographic effects of a typical regional ridge. Because of the randomness of the height distribution in the adjacent ridge, a neighboring ridge with an elevation equivalent to that of the central ridge was observed in a typical specimen. However, the adjacent ridge did not experience significant ground motion during the earthquake, which is an interesting phenomenon warranting further investigation. However, there were disparities between the acceleration and GMAF elevation charts upon comparison. Therefore, a combination of acceleration and the GMAF is essential in the structural design process.

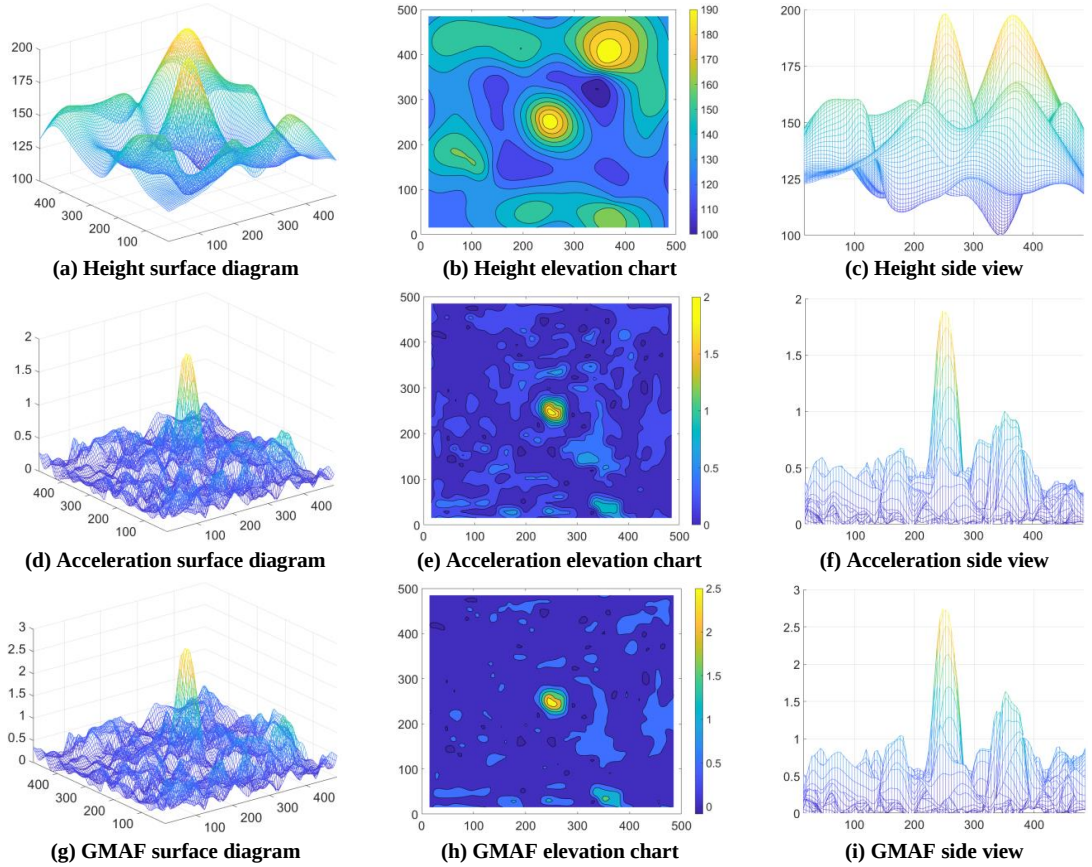

(a) Height surface diagram (b) Height elevation chart (c) Height side view

(d) Acceleration surface diagram (e) Acceleration elevation chart (f) Acceleration side view

(g) GMAF surface diagram (h) GMAF elevation chart (i) GMAF side view

Figure 18. Regional topographic effect of a typical regional ridge (units: m for height; m/s^2 for acceleration)

5.3. Original and Higher Ridges

The last situation occurs when the original ridge is surrounded by higher ridges, as shown in Figure 19 provided the analysis results. The height of the original ridge was 100 m, and the heights of the adjacent ridges were randomly generated from 100 to 150 m. The range of maximum peak acceleration of the ridged top was from 1.44 m/s^2 to 2.08 m/s^2, indicating that adjacent higher ridge would influence on the vibration intensity of the original ridge. Notably, the maximum acceleration was observed at the summit of the central ridge rather than at the higher ridge. This phenomenon is the same as the rule described in Section 4.3, which is important for structural seismic design. Unfortunately, we were unable to conduct further analyses because of the reasons due to computational limitations.

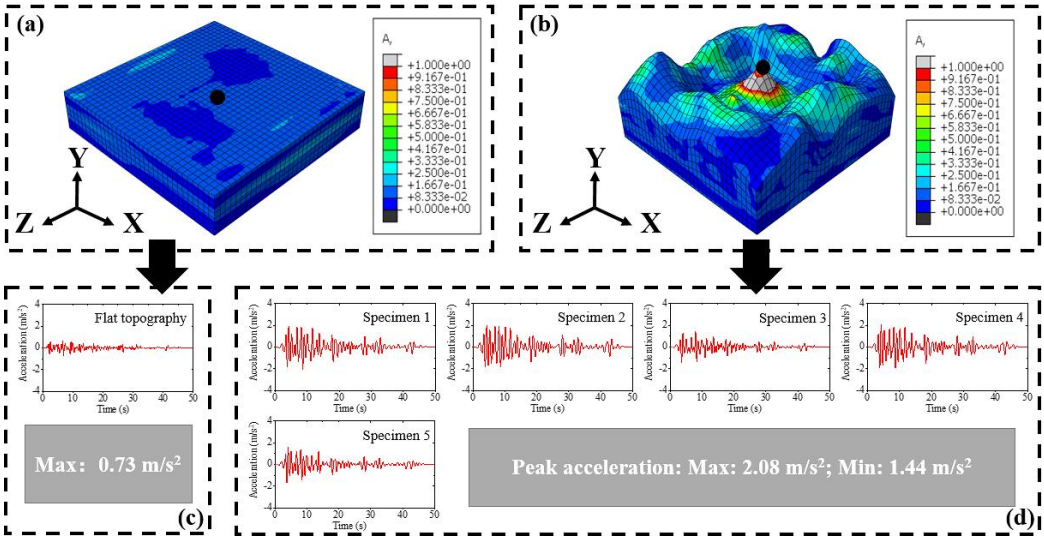

Figure 19. Acceleration time-history curve comparison of 5 specimens

Figure 20 shows the regional topographic effect of a typical regional ridge with the original and higher ridges. The maximum value of the EAMF was observed at the center, which coincided with that of the acceleration. Despite the complexity of the regional topography, the whipping effect was only evident in the central area. Therefore, it is advisable to minimize the utilization of this region in structural seismic designs. The maximum GMAF value of the central ridge was 2.98 and lower than that of the isolated ridge (3.52). The interaction between the original and higher ridges can mitigate topographic effects.

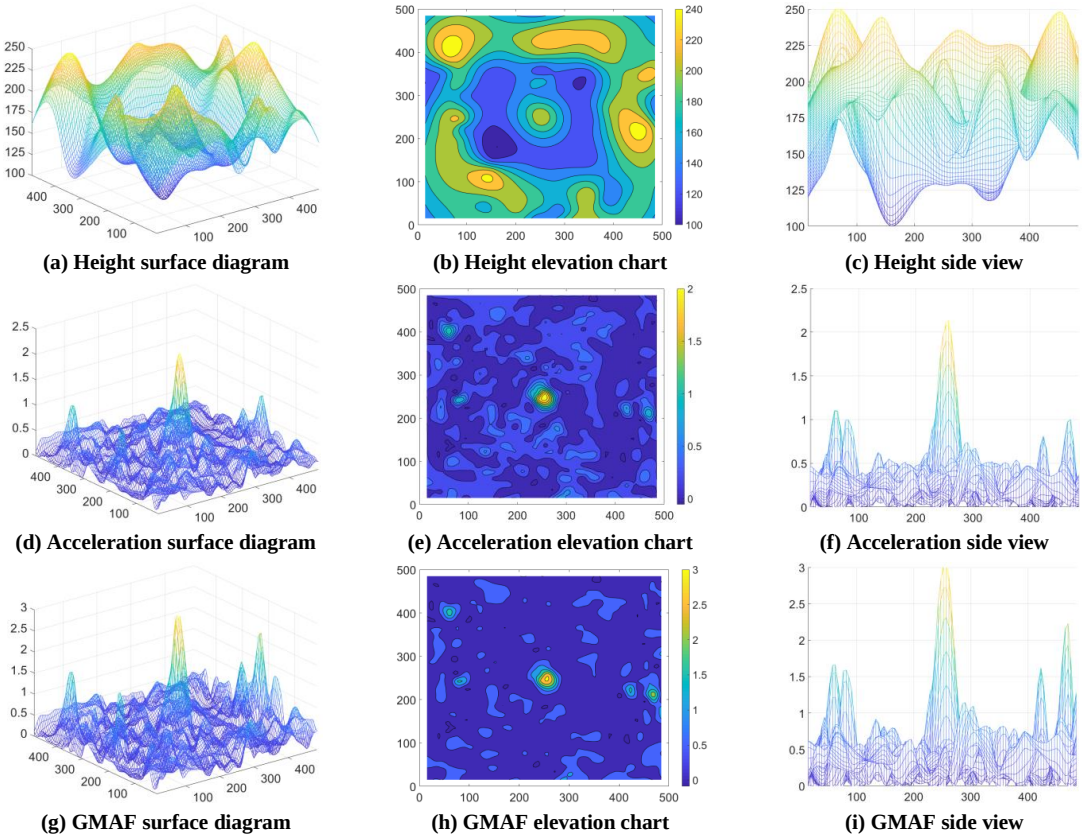

(a) Height surface diagram **(b) Height elevation chart** **(c) Height side view**

(d) Acceleration surface diagram **(e) Acceleration elevation chart** **(f) Acceleration side view**

(g) GMAF surface diagram **(h) GMAF elevation chart** **(i) GMAF side view**

Figure 20. Regional topographic effect of a typical regional ridge (units: m for height; m/s^2 for acceleration)

Across all the regional configurations, the peak response consistently occurred at the central ridge, confirming that the highest point remained the most critical location. The dispersion of the GMAF values among different random realizations indicates that the surrounding terrain redistributes wave energy and introduces variability. This suggests that seismic design in mountainous regions should consider a broader topographic context rather than the local ridge geometry alone.

6. Discussion

The findings of this study are broadly consistent with those of previous works, indicating that topographic amplification is highly sensitive to local geometry and material properties. Prior studies have primarily examined isolated ridges or simplified slope configurations, reporting significant crest amplification that varies with the slope angle, height, and soil stiffness. The results of the present study confirm these general trends for single-ridge topography, while extending the analysis to more complex multi-ridge settings. A key contribution of this study is the quantification of ridge interaction effects, which demonstrates that amplification factors derived from isolated features tend to overestimate responses when a ridge is embedded within a regional topographic context. The directional dependence observed here, particularly the greater dispersion and magnitude of the vertical amplification, aligns with earlier reports that vertical ground motion can be comparably or even more affected by topography than horizontal motion. Previous investigations have largely focused on two-dimensional profiles or single three-dimensional features, whereas this study systematically evaluated the compounded effects in double-ridged and randomly generated regional topographies. The consistent reduction in crest amplification by the surrounding terrain, regardless of whether the adjacent ridges are higher or lower, represents a phenomenon that has received limited attention in the literature. The comparisons in the present study highlight the need for caution when extrapolating single-ridge results to realistic mountainous terrain, and support direction-specific and context-dependent amplification assessments in seismic design practice.

7. Conclusion

This study systematically investigated the influence of regional topography on ground motion amplification factors using three-dimensional finite element simulations validated against centrifuge experimental data. The modeling framework incorporates image-recognition-based topographic surface generation and viscoelastic artificial boundaries, enabling a realistic representation of both idealized and complex multiridge terrains.

This analysis revealed several key findings. For a single-ridged topography, GMAFs are sensitive to the elastic modulus, ridge height, and slope angle. The peak horizontal acceleration varies nonmonotonically with the elastic modulus owing to shifts in the ridge resonance frequencies, whereas increasing the ridge height produces a pronounced whipping effect. The vertical GMAFs consistently exceeded the horizontal components and exhibited greater dispersion, indicating that vertical amplification must be assessed separately. Furthermore, the GMAFs for acceleration, velocity, and displacement exhibited distinct behaviors, likely attributable to their differing sensitivities to the frequency components of the seismic waves; however, the underlying physical mechanisms warrant further investigation. Double-ridged analyses demonstrate that adjacent ridges consistently reduce crest amplification relative to the isolated case through scattered wave-field interactions. Closer spacing intensified this mitigation, whereas increasing the height of the adjacent ridge partially recovered the original response. Vertical GMAF maxima frequently occurred on the flanks rather than at the crest, further confirming the distinct behavior of vertical ground motion. For regional topography, the peak response remained concentrated at the highest central ridge, yet the GMAF values were consistently lower than those of an equivalent isolated ridge, with the dispersion among randomly generated topographies highlighting the variability introduced by the surrounding terrain.

These findings have direct implications for seismic designs in mountainous regions. Amplification factors derived from isolated topographic features may overestimate the crest response in complex terrain. Pronounced directional differences necessitate separate horizontal and vertical GMAF evaluations. The significant influence of ridge interactions further suggests that a probabilistic framework is suitable for site-specific hazard assessments. Future work should extend the analysis to include material heterogeneity, three-dimensional incident wave fields, larger regional domains, frequency-dependent scattering, and energy dissipation mechanisms governing the differences between acceleration, velocity, and displacement amplification.

8. Declarations

8.1. Author Contributions

Conceptualization, Y.W.; methodology, Q.L. and D.W.; software, Q.L. and M.Z.; formal analysis, Q.L.; resources, S.Z. and J.X.; data curation, S.Z.; writing—original draft preparation, Q.L.; writing—review and editing, J.X.; supervision, Y.W.; funding acquisition, J.X. All authors have read and agreed to the published version of the manuscript.

8.2. Data Availability Statement

The data presented in this study are available on request from the corresponding author.

8.3. Funding and Acknowledgments

The authors are grateful for the financial support received from the National Key Research and Development Program of China (2025YFE0117900), Science and Technology Department of Sichuan Province (2024JDRC0101), Open Fund of the National Science Center for Earthquake Engineering (No. 2025KFB1001), Sichuan Provincial Department of Housing and Urban-Rural Development Science and Technology Project (KJ25006 and KJ25002), and Research Project of Sichuan Architectural Design and Research Institute (KYYN2025020 and KYYN2025018), Science and Technology Project of Sichuan Huaxi Group (HXKX2026015).

8.4. Conflicts of Interest

The authors declare no conflict of interest.

9. References

[1] Xiong, J., Tang, C., Tang, H., Chen, M., Zhang, X., Shi, Q., Chang, M., Gong, L., Li, N., & Li, M. (2022). Long-term hillslope erosion and landslide–channel coupling in the area of the catastrophic Wenchuan earthquake. Engineering Geology, 305, 106727. doi:10.1016/j.enggeo.2022.106727.

[2] Bowden, D. C., & Tsai, V. C. (2017). Earthquake ground motion amplification for surface waves. Geophysical Research Letters, 44(1), 121–127. doi:10.1002/2016GL071885.

[3] Qiao, H., Dai, Z., Du, X., Wang, C., Long, P., & Jiao, C. (2023). Parametric study of topographic effect on train-bridge interaction of a continuous rigid frame bridge during earthquakes. Bulletin of Earthquake Engineering, 21(1), 125–149. doi:10.1007/s10518-022-01532-7.

[4] Zhao, S., Luo, Q., Tang, Y., Xia, J., Li, Y., & Zhang, M. (2025). Numerical Analysis of Ground Motion Topographic and Geological Effect: A Case Study of MOXI Platform. Civil Engineering Journal (Iran), 11(9), 3554–3573. doi:10.28991/CEJ-2025-011-09-01.

[5] Shen, H., Liu, Y., Li, X., Li, H., Wang, L., & Huang, W. (2025). The combined amplification effects of topography and stratigraphy of layered rock slopes under vertically and obliquely incident seismic waves. Soil Dynamics and Earthquake Engineering, 193, 109331. doi:10.1016/j.soildyn.2025.109331.

[6] Luo, Y., Fan, X., Huang, R., Wang, Y., Yunus, A. P., & Havenith, H. B. (2020). Topographic and near-surface stratigraphic amplification of the seismic response of a mountain slope revealed by field monitoring and numerical simulations. Engineering Geology, 271, 105607. doi:10.1016/j.enggeo.2020.105607.

[7] Zaoui, M. A. I., Derras, B., & Régnier, J. (2025). Impact of several site-condition proxies and ground-motion intensity measures on the spectral amplification factor using neuro-fuzzy approach: an example on the KiK-Net dataset. Natural Hazards, 121(7), 8703–8732. doi:10.1007/s11069-025-07151-0.

[8] Tripe, R., Kontoe, S., & Wong, T. K. C. (2013). Slope topography effects on ground motion in the presence of deep soil layers. Soil Dynamics and Earthquake Engineering, 50, 72–84. doi:10.1016/j.soildyn.2013.02.011.

[9] Lee, M. G., Sun, C. G., Kim, H. S., Choo, Y. W., & Cho, H. I. (2025). Experimental study on site and topographic effects on seismic responses in single-sided slopes. Engineering Geology, 345, 107868. doi:10.1016/j.enggeo.2024.107868.

[10] Li, Y., Wang, G., & Wang, Y. (2022). Parametric investigation on the effect of sloping topography on horizontal and vertical ground motions. Soil Dynamics and Earthquake Engineering, 159, 107346. doi:10.1016/j.soildyn.2022.107346.

[11] Tai, D., Qi, S., Zheng, B., Luo, G., He, J., Guo, S., Zou, Y., & Wang, Z. (2024). Effect of excitation frequency and joint density on the dynamic amplification effect of slope surface on jointed rock slopes. Engineering Geology, 330, 107385. doi:10.1016/j.enggeo.2023.107385.

[12] Wang, W., Li, D. Q., Liu, Y., & Du, W. (2021). Influence of ground motion duration on the seismic performance of earth slopes based on numerical analysis. Soil Dynamics and Earthquake Engineering, 143, 106595. doi:10.1016/j.soildyn.2021.106595.

[13] Wang, H., Cui, S., Pei, X., Zhu, L., Yang, Q., & Huang, R. (2022). Geology amplification of the seismic response of a large deep-seated rock slope revealed by field monitoring and geophysical methods. Environmental Earth Sciences, 81(7), 191. doi:10.1007/s12665-022-10314-y.

[14] Zhang, N., Lu, H., Zhang, Y., Pan, J., Shen, F., Dai, D., & Gao, Y. (2026). Impact of multi-canyon topography on seismic ground motions under SH waves in mountainous areas. Applied Mathematical Modelling, 150. doi:10.1016/j.apm.2025.116336.

[15] Bouckovalas, G. D., & Papadimitriou, A. G. (2005). Numerical evaluation of slope topography effects on seismic ground motion. Soil Dynamics and Earthquake Engineering, 25(7-10), 547-558. doi:10.1016/j.soildyn.2004.11.008.

[16] Liu, J., Tan, H., Bao, X., Wang, D., & Li, S. (2019). Seismic wave input method for three-dimensional soil-structure dynamic interaction analysis based on the substructure of artificial boundaries. Earthquake Engineering and Engineering Vibration, 18(4), 747–758. doi:10.1007/s11803-019-0534-5.

[17] Wang, F., Song, Z., Liu, Y., & Luo, B. (2021). Seismic wave input method for high earth dams considering the transmission amplification effect of the bedrock–overburden interface. Computers and Geotechnics, 130, 103927. doi:10.1016/j.compgeo.2020.103927.

[18] Liu, J., Bao, X., Wang, D., Tan, H., & Li, S. (2019). The internal substructure method for seismic wave input in 3D dynamic soil-structure interaction analysis. Soil Dynamics and Earthquake Engineering, 127, 105847. doi:10.1016/j.soildyn.2019.105847.

[19] Huang, J. qi, Du, X. li, Zhao, M., & Zhao, X. (2017). Impact of incident angles of earthquake shear (S) waves on 3-D non-linear seismic responses of long lined tunnels. Engineering Geology, 222, 168–185. doi:10.1016/j.enggeo.2017.03.017.

[20] Sun, Z., Kong, L., Guo, A., Xu, G., & Bai, W. (2019). Experimental and numerical investigations of the seismic response of a rock–soil mixture deposit slope. Environmental Earth Sciences, 78(24), 1–14. doi:10.1007/s12665-019-8717-y.

[21] GB 50011-2010. (2016). Code for seismic design of buildings. China Architecture & Building Press, Beijing, China. (In Chinese).